




Influence of fiber alignment on pseudoductility and microcracking in a cementitious carbon fiber composite material

Matthias Rutzen · Philipp Lauff · Roland Niedermeier · Oliver Fischer ·
Manuel Raith · Christian U. Grosse · Ursula Weiss · Malte A. Peter ·
Dirk Volkmer 

Received: 17 October 2020 / Accepted: 7 February 2021
© The Author(s) 2021

Abstract This research examines the effect of fiber alignment on the performance of an exceptionally tough 3D-printable short carbon fiber reinforced cementitious composite material, the flexural strength of which can exceed 100 N/mm^2 . The material shows pseudoductility caused by strain-hardening and microcracking. An extrusion-based manufacturing process allows accurate control over the spatial alignment of the fibers' orientation, since extrusion through a tight nozzle leads to nearly unidirectional alignment of the fibers with respect to the directional movement of the nozzle. Specimens were investigated using mechanical tests (flexural and tensile load), augmented by non-

destructive methods such as X-ray 3D computed tomography and acoustic emission analysis to gain insight into the microstructure. Additionally, digital image correlation is used to visualize the microcracking process. X-ray CT confirms that about 70% of fibers show less than 10° deviation from the extrusion direction. Systematic variations of the fiber alignment with respect to the direction of tensile load show that carbon fibers enhance the flexural strength of the test specimens as long as their alignment angle does not deviate by more than 20° from the direction of the acting tensile stress. Acoustic emission analysis is capable of evaluating the spatiotemporal degradation behavior during loading and shows consistent results with the microstructural damage observed in CT scans. The strong connection of fiber alignment and flexural strength ties into a change from ductile to brittle failure caused by degradation on a microstructural level, as seen by complementary results acquired from the aforementioned methods of investigation.

Supplementary Information The online version contains supplementary material available at <https://doi.org/10.1617/s11527-021-01649-2>.

M. Rutzen · D. Volkmer (✉)
Chair of Solid State and Materials Chemistry, University
of Augsburg, 86159 Augsburg, Germany
e-mail: dirk.volkmer@physik.uni-augsburg.de

P. Lauff · R. Niedermeier · O. Fischer
Chair of Concrete and Masonry Structures, Technical
University of Munich, 80333 Munich, Germany

M. Raith · C. U. Grosse
Chair of Non-Destructive Testing, Technical University
of Munich, 81245 Munich, Germany

U. Weiss · M. A. Peter
Research Unit Applied Analysis, University of Augsburg,
86159 Augsburg, Germany

Keywords Microcracking · Fiber reinforcement · X-ray CT · Tensile properties · 3D printing · Strain-hardening



1 Introduction

Unreinforced cementitious materials are well known for possessing high compressive strength while being weak under flexural and tensile loads. Such loads bring about a very sudden brittle failure, meaning a single macroscopic crack leading to instant destruction of the loaded specimen. Common technological solutions to mitigate poor behavior under tensile load and suddenness of the failure include the introduction of reinforcing steel bars or alternatively various kinds of fibers. Most reinforcement fibers are made of minerals, glass, polymer, steel or carbon [1–5]. Fiber reinforcement does not necessarily lead to improvement of tensile strength, as the fibers' mechanical properties might be unsuitable; they may be below the critical fiber length or the bond between fiber and matrix might not be strong enough to support full transition of loads from one material to another, which has a significant impact on the macroscopic response [6]. Such composites will show a slightly improved toughness, as the fibers are pulled out after cracks started separating the matrix [4, 7]. Generally, such systems are labeled as 'Fiber Reinforced Concrete (FRC)' in the literature [8]. However, tailoring chemical compatibility and micromechanical parameters of cementitious materials towards fiber reinforcement allows for the creation of a material that no longer shows brittle single crack failure but rather a significant pseudoductility. This behavior shows itself in a strain-hardening response beyond purely elastic deformation capabilities. Such composites also show enhanced tensile and flexural strength. These materials have been dubbed 'Engineered Cementitious Composites (ECC)' or 'Strain-Hardening Cementitious Composites (SHCC)' in literature. [9, 10]. The pseudoductile behavior is known to be attributed to a change of the microstructure. At stresses beyond the linear-elastic phase, small-scale cavities appear. Instead of combining into a macroscopic crack and critically failing instantly (brittle fracture) or a slow but continuous growth of the cavities leading to a decrease in stress (strain-softening), two effects combine. (a) The presence of the fibers stops the growth of the cavities and (b) the stiff fibers begin to transmit the stresses, which leads to an overall increase in the stress–strain response (strain-hardening). Thus, once the material undergoes strain-hardening, a large number of tightly spaced microcracks appear and

those cracks are bridged by the fibers. Therefore, such materials are not only characterized by an increase in tensile and flexural strength but also by a considerably higher capacity for deformation. [11–13]. Typically these composites are made using polymer fibers, i.e. polyvinylalcohol (PVA) and high-density polyethylene (HDPE) fibers in particular [14]. Recent research has shown that addition of stiffer and stronger fibers, such as carbon fibers, coupled with the usage of an extrusion-based alignment process, a cementitious composite, which exhibits a flexural strength in excess of 100 N/mm^2 , can be created [15]. Such materials are highly interesting for applications in additive manufacturing ('3D printing') [16]. The extreme flexural strength makes the composite an enticing material to reduce the amount of continuous steel reinforcement necessary, as some tensile load can be handled by the cementitious composite itself. Opposed to reinforcing steel, carbon fibers show no tendency to corrode or degrade under atmospheric conditions, leading to a higher expected lifetime of the final structure. The low crack widths also lead to other desirable traits, such as high durability by hindered diffusion of aggressive compounds into the matrix and self-healing properties [17–20]. Reinforcement with carbon fibers grants the material a degree of electrical conductivity, which allows the material to be potentially used in heating elements [21] or in the field of structural health monitoring [22].

The aforementioned extrusion process leads to a nearly unidirectional alignment of the fibers. As the fibers are pushed through a tight nozzle, their alignment will follow the movement direction of the nozzle. The effectiveness of this principle has been shown in prior research on Portland cement [15, 16], aluminate cement and mixed cementitious binders [23] and also with polymer resins [24–26]. The material has been successfully used to create 3D printed samples with high flexural strength [16, 27].

While the first serious research in the field of additive manufacturing in the construction sector can be traced back to the 1990s [28, 29], such methods had problems scaling up to structural levels and penetrating the market up until recently [30–32]. Especially the fact that reinforcing materials still have to be manually inserted into the structures and cannot be automatically incorporated into the printing process is a problem that has only recently been acknowledged by research [33]. As the process described in this paper



is analogous to the 3D-printing method commonly described as ‘Liquid Deposition’, in which strands of a flowable material are deposited layer by layer to create a desired shape after hardening, this poses an elegant solution to this problem, as no external reinforcement is needed and a fully automatic process is realized. As fiber alignment follows printing direction, the production of structural members specifically designed to withstand complex loading scenarios by matching up printer movement to occurring principle tensile stress paths should be feasible.

One specific problem that occurs when using inherently anisotropic materials such as fibers is the fact that exact knowledge and control of fiber alignment plays a huge role in the interpretation of experimental results. As traditional mold-casting techniques do not allow for customization in this regard, little information between the direct correlation of fiber alignment and material behavior can be found in actual data. Applying non-destructive testing techniques is ambitious due to the high degree of heterogeneity and anisotropy [34]. This research focuses on the evaluation of fiber-matrix interaction by correlating macroscopic methods such as mechanical testing with highly localized non-destructive methods of analysis, such as digital image correlation (DIC), ultrasound (US), acoustic emission analysis (AEA) and X-ray 3D computed tomography (X-ray CT).

2 Materials and methods

2.1 Overview and scope

This publication aims to shed light on the correlation between the general response of a carbon-fiber reinforced composite material during mechanical testing (e.g. ultimate strength and capacity for deformation under flexural and tensile load) and the mechanism of the resulting damage, in particular the relation between in-plane fiber alignment and the resulting microcracking behavior.

The feasibility of measuring fiber orientation and damage indicators (especially in-volume growth of microcracks) using high resolution X-ray CT coupled with advanced segmentation techniques on miniature bending beams is tested and the data is correlated to macroscopic mechanical behavior. We intend to show

the reasons behind a transition from ductile to brittle behavior in the material as fiber alignment starts to deviate from the direction of the acting tensile load.

Alongside the CT, other powerful techniques are used to obtain a more complete picture of the fracture process. In particular DIC for in-situ observations of surface crack growth (using larger dogbone-shaped samples) [35] and acoustic emission analysis (using miniature bending beams) for further analysis of failure mechanism by means of frequency analysis are applied. Setup of miniature beams during 3-point bending tests and definitions of the coordinate system and angles used can be seen in Fig. 1.

2.2 Sample preparation of miniature beams

All test specimens were prepared as described in a previous publication of our working group [15], which describes a formulation tailored to allow for superior fiber dispersion and bond strength between fiber and matrix. The cement used was a CEM I 52.5 R type supplied by Schwenk Zement KG, sourced from the cement plant Karlstadt. Carbon fibers were purchased from Teijin Ltd. being commercialized under the product name Tenax-J HT C261. The carbon fibers, which are uniformly chopped down to a length of 3 mm, have the following specifications: diameter: 7 μm , tensile strength: 4000 N/mm², Young’s modulus: 238 GPa. Prior to usage in the cement paste, the fibers were oxidatively heat treated in an open furnace at 425 °C for 2 h to remove the sizing and to oxidize the carbon fiber’s surface, improving wettability and fiber-matrix bonding [15, 36, 37]. Barium sulfate is added to increase the X-ray absorption of the cementitious matrix and thus to increase the electron density contrast with respect to other embedded materials, especially the carbon fibers [38]. All components used for sample preparation are given in Table 1.

Cement (CEM I 52.5 R, Schwenk Zement KG, Ulm, Germany), silica fume (EFACO, Egyptian Ferro-Alloys Company, Edfu, Egypt) and barium sulfate (Acros Organics, Geel, Belgium) are added into the mixing container and dry mixed by hand. Deionized water and superplasticizer (MasterGlenium ACE 430, BASF Construction Solutions GmbH, Trostberg, Germany) are premixed in a glass beaker. The liquid components are mixed into the binder using a Heidolph Hei-TORQUE Precision 400 overhead mixer (Heidolph Instruments GmbH & CO. KG,

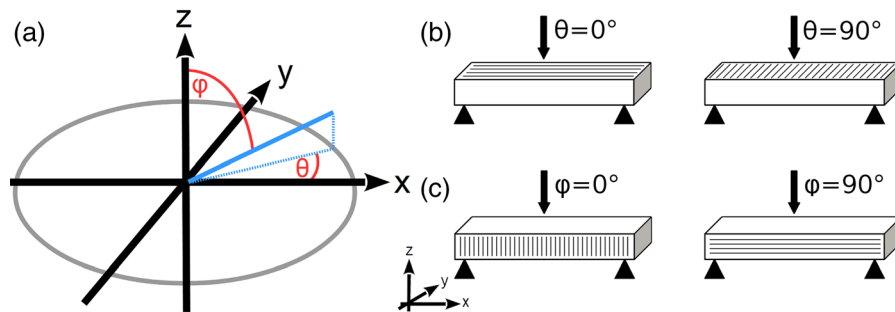


Fig. 1 Setup of sample and description of angles during testing and alignment analysis. **a** Coordinate system with a hypothetical angled object. The angle between x - and y -axis describes the in-plane alignment (called θ -angle or yaw). The angle coming from the positive z -axis and the object to be described is the out-of-plane alignment (called φ -angle or pitch). **b** Orientation of

bending beams within the coordinate system. Beams are aligned along their length with the x -axis and along their width with the y -axis. **b** Subsequently, fibers that lie in direction of the tensile force occurring during bending are labeled as having a θ -angle of 0° . **c** φ -angles describe the upward and downward tilt, with an angle of 90° being fully parallel to the x - y -plane

Table 1 Raw materials and mixture design for the production of the cementitious composite material

| Raw material | Dose by weight (wt%) | Density (g/cm ³) | Dose by volume (vol%) | Mixture design (kg/m ³) |
|--------------------------------|----------------------|------------------------------|-----------------------|-------------------------------------|
| CEM I 52.5 R | 58.2 | 3.10 | 41.2 | 1276.4 |
| Silica fume EFACO | 20.0 | 2.25 | 19.5 | 438.6 |
| Barium sulfate | 4.6 | 4.50 | 2.2 | 100.9 |
| Deionized water | 14.3 | 1.00 | 31.4 | 313.6 |
| Master Glenium ACE 430 | 2.9 | 1.11 | 5.7 | 63.6 |
| Dosage per vol% fiber content: | | | | |
| Tenax-J HT C261 | 0.803 | 1.76 | 1.0 | 17.6 |

Volumetric dosage of fibers is based on the calculated total volume of the fresh paste

Schwabach, Germany) at 400 RPM for 90 s until all solids are dispersed homogenously. After scraping undispersed remains off the stirrer and container walls, the paste is mixed again for 90 s at 2000 RPM. After this step, the carbon fibers (Tenax-J HT C261, 3 mm in length, 7 μ m in diameter, Teijin Ltd., Tokyo, Japan) are admixed into the paste and stirred at 70 RPM for 30 s. The fiber-reinforced paste is extruded through a disposable 10 mL syringe with a nozzle diameter of 2 mm (B. Braun Melsungen AG, Melsungen, Germany). Fibers were found to stay mostly intact throughout the process with only very little reduction in length visible. Some further information is included in the Supplementary Material to this paper. Admixing the fibers leads to a very noticeable increase in viscosity of the paste. Flow table tests using a Hägermann table (cone diameter of 100 mm) show a flow value of 181 mm for the paste without fibers,

152 mm for the paste containing 1 vol% of fibers and 117 mm for the paste containing 3 vol% of fibers after 15 shocks.

This process leads to an almost unidirectional fiber alignment along the movement path of the nozzle; the fiber orientation within representative volume elements of the test specimens are quantified by X-ray CT measurements. To obtain samples with a specific in-plane fiber alignment, guide templates assisting the extrusion of the cement paste along predefined lines were printed and put under a transparent piece of polycarbonate plastic. The syringe was guided along the lines of the template, producing a slab measuring approximately $100 \times 50 \times 3$ mm. The process can be seen in Fig. 2.

The slabs were allowed to harden for 24 h at 100% relative humidity by storing it within a sealed desiccator over water. After this period, it was stored under

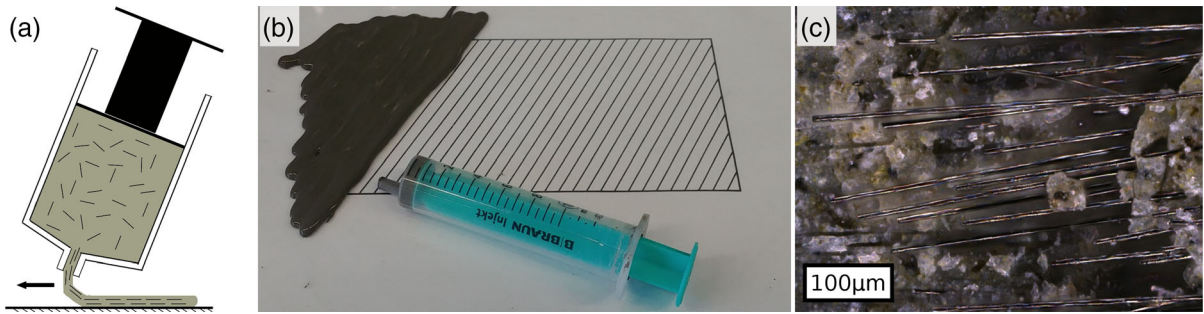


Fig. 2 Principle of the fiber-alignment process. **a** Extrusion of the composite material through the tight nozzle of a syringe leads to unidirectional orientation of the fibers. The fibers' long axis becomes aligned parallel to the path of movement.

b Guiding a syringe along the path of an angled template, samples with specific alignment can be created. **c** Optical microscope image of aligned fibers in the crack of a test specimen after failure

water for another 6 days. Following this, the sample was allowed to dry and stored within a sealed desiccator at 59% relative humidity for 21 days. The humidity level was adjusted by maintaining a reservoir of oversaturated sodium bromide solution within the desiccator. All tests were carried out after 28 days of storage. After 7 days of storage, the samples were manually lapped down to a thickness of approximately 2 mm using tungsten carbide powder. This procedure also made sure that remaining roughness of the sample surface was eliminated. For 3-point bending tests the slabs were then cut into miniature beam-shaped specimens of the dimensions $60 \times 4 \times 2$ mm using a Buehler IsoMet low speed saw (Buehler, Lake Bluff, IL, USA).

2.3 3-Point bending tests on miniature beams

The flexural strength of miniature beams was tested using a ZwickRoell zwickiLine Z5.0 universal testing machine with a 5 kN load cell attached. Testing was carried out in deformation controlled mode at 1 mm/min. The force (F) measured by the machine is converted into flexural stress ($f_{ct,fl}$) using the following equation:

$$f_{ct,fl} = 3 \cdot F \cdot l / 2 \cdot w \cdot h^2 \quad (1)$$

where l is the span between the supports (set up at 50.0 ± 0.1 mm), w and h are the width and height of the sample, respectively. Dimensions of the sample were determined using a digital caliper prior to testing. Unless specified otherwise, strain (ε) was calculated from deflection (D) at the center of the miniature beam according to the following equation:

$$\varepsilon = 6 \cdot D \cdot \frac{h}{l^2} \cdot 100 \% \quad (2)$$

where h is the height of the sample and l is the span between the supports (set up at 50.0 ± 0.1 mm).

2.4 Visualization of crack patterns using digital image correlation

Since the small size of the miniature bending beams severely limits the usage of more sensitive deformation measurement tools such as strain gauges, larger test specimens are produced according to the process described in Sect. 2.2 using a 3D-concrete-printer developed at the Technical University of Munich. The tests are carried out under uniaxial tensile load using dogbone-shaped samples with a carbon fiber content of 1% by volume. They measure 450 mm in length, the cross section at the midpoint of the specimen measures 50×50 mm, the bone then expands towards both ends to a cross section of 100×50 mm (Fig. 3a). The specimens are tested with clamped ends in order to minimize eccentric loading caused by crack development and displacement of the center line (Fig. 3b). To achieve this, the dogbone is glued with duromer adhesive MC-DUR 1280 (MC-Bauchemie Müller GmbH & Co. KG, Bottrop, Germany) into bearing plates connected to the testing machine.

As the degradation process of the material beyond the linear-elastic region is strongly characterized by small and very localized deformation processes, strain gauges and DIC are used to provide a more accurate description of sample deformation. Especially DIC is a

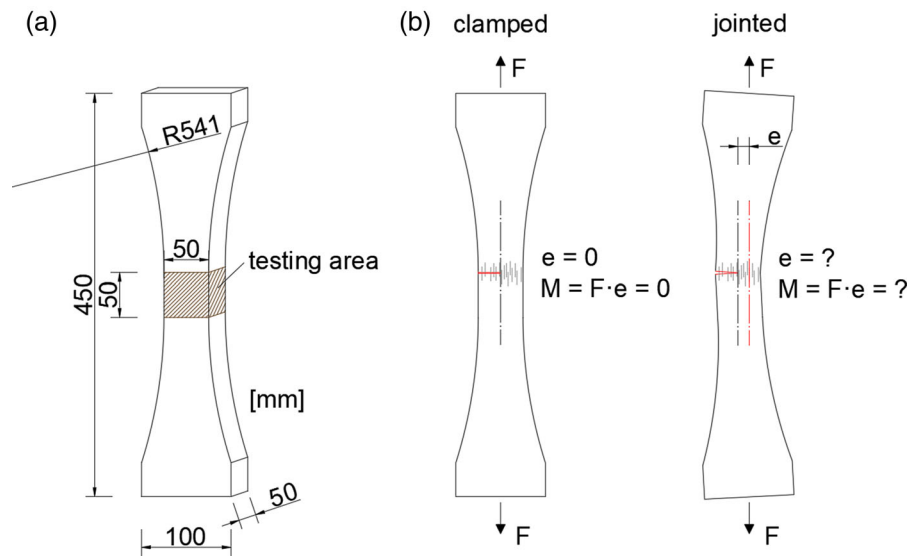


Fig. 3 Dimensions of dogbone-shaped specimens used for tensile testing. The region of interest is shaded in grey (a) and generated moment influence of non-clamped specimen ends during testing with crack development (b)

powerful tool to visualize the formation and growth of cracks across a whole specimen.

The dogbone-shaped specimens were tested using a SCHENK 400 universal testing machine with a 400 kN load cell attached. The testing program was deformation controlled at 0.18 mm/min. The maximum force (F) measured by the load cell is converted into tensile strength (f_{ct}) by normalizing force to the load bearing area (A) of the cross section according to:

$$f_{ct} = F/A \quad (3)$$

Deformation was measured using strain gauges FLAB-3-11 (Tokyo Measuring Instruments Laboratory Co., Ltd., Tokyo, Japan) and a GOM Aramis stereocamera (GOM GmbH, Braunschweig, Germany).

Additionally, flexural strength is tested on beam-shaped specimens in a 3-point-bending setup. The dimensions are an elongated version of the standardized beam referenced in DIN EN 196-1. They measure $40 \times 40 \times 220$ mm, the effective span is 180 mm and the load is applied at the midpoint. The standardized beam specimens were prepared with a carbon fiber content of 2% by volume, as the simpler geometry allowed for printing with a higher fiber content. All specimens were produced according to the mixture design given in Table 1.

Using photogrammetry combined with DIC, local strain development on the surface can be made visible and crack widths can be measured. Even cracks not visible to the naked eye can be visualized without further time consuming preparation (e.g. dye penetration) [39]. For this reason, DIC has been widely used to characterize fracture processes in construction materials [40, 41]. The specimens are prepared by applying white paint on the surface and spraying a random dot pattern with a black graphite lacquer on top. During testing, the prepared area is photographed continuously. The first picture taken is used as reference in an unloaded stage to which the following pictures are correlated. To track displacements, the area is divided into small facets and due to the random dot pattern, each facet has its own fingerprint and can be found in every picture. The movement of the facets is used to calculate real displacements and strains.

2.5 X-ray 3D computed tomography (X-ray CT) measurements

X-ray CT measurements were performed on miniature beam samples using a Phoenix nanotom m scanner (GE Inspection Technologies LP, Lewistown, PA, USA). One scan comprised of 2000 single images taken with an integration time of 2000 ms. The X-ray was created using an acceleration voltage of 70 kV

and a beam current of 190 μA . The voxel size for all scans was 1.9 μm . To obtain as much information about the fracture process zone as possible, each sample was scanned four times at different positions along its length. Reconstruction was carried out for each partial scan using the software Phoenix datoslx. The reconstruction process was calibrated using the datoslx module 'agc' ('automatic geometry calibration') and a ring-artifact reducing filter and a Gaussian smoothing filter were applied. The reconstructed scan was saved into raw format and imported into the metrology software Dragonfly Pro 4.1 (Object Research Systems (ORS) Inc., Montreal, Canada) for analysis. The resolution of the scan was scaled down by a factor of 2 from the original voxel size of 1.9 μm to 3.8 μm during the import process to decrease computational demand. There, the reconstructed multi-scans were aligned using the stitching functions of ORS Dragonfly in the overlapping regions.

2.6 X-ray CT segmentation procedure

The main challenge during the segmentation procedure is the fact that the contrast between carbon fibers and cementitious matrix is rather low and the greyscale values of each material overlap instead of being separated into singular peaks in the histogram. Thus, a segmentation procedure, which is purely based on threshold values for each material, is not feasible. Instead, the scan is filtered through a local equalization algorithm, which emphasizes local deviation of greyscale values. As there is very little deviation within the fibers themselves, they will appear as black lines, within a bright (albeit noisy) matrix. The black portion of the locally equalized picture can then be segmented by manually defining a threshold value. Remaining artifacts and noise can be removed by performing a connectivity analysis and transforming connected voxels into discrete objects. By deleting objects that do not fit the geometric parameters of a fiber from the segmentation (e.g. spherical objects with an aspect ratio approaching 1 and objects which deviate too far from the fibers geometrical volume), a good fit of segmented voxels to the fiber material in the scan can be achieved. Segmentation strategies based on similar principles are often found in the literature when purely grey value-based segmentation fails. [42, 43].

Microcracks were also segmented from images, which were passed through the local equalization

filter. Since cracks are relatively discrete objects, they were not segmented using a global greyscale threshold, but rather by using a region-filling tool, which adds a connected region of the same greyscale value to the current segmentation. Objects that were falsely identified as belonging to a crack (e.g. fibers bridging through the crack) were removed by skeletonizing and then dilating the segmented region.

2.7 Acoustic emission analysis

Acoustic emission testing on small specimens made of various fiber reinforced materials was conducted by several working groups in the past. These experiments include a variety of different materials such as SiC reinforced ceramics [44], glass-fiber reinforced polymers (GFRP) [45] and steel-fiber reinforced concrete [46]. The majority of publications consider carbon-fiber reinforced polymers (CFRP) and attempt the determination of failure mechanics [47, 48]. To achieve this, source localization frequency analysis and event counting methods are applied. Within this study, acoustic emission testing is used to monitor the damage evolution in miniature beam specimens with a carbon fiber content of 1 vol% under static three-point bending load [49]. The objective was the spatial and temporal resolution of crack formation and fiber failure. Four small-sized resonant acoustic emission (AE) sensors were attached to the specimen using hot adhesive. Due to the resonant frequency response of the used AE sensors and the requirement to perform a frequency analysis, waveforms were recorded by a Laser-Doppler-Vibrometer (LDV) in addition. The used LDV provided a quasilinear frequency response function between 30 kHz and 24 MHz and a resolution of 0.1 $\text{pm}/\text{Hz}^{0.5}$. Load was applied using a Wolpert 10 kN load frame and a 500 N load cell. Acoustic waves, emerging from fiber breakage or matrix fracture due to mechanical load and propagating through the specimen were detected by the AE sensors and the LDV. The induced voltage signal was then transferred to an Elsys eight channel data acquisition system, where it was digitized at 20 MHz sampling rate. In Fig. 4 an overview of the experimental setup is provided. Data analysis was done with own code based on MATLAB®.

In order to obtain the source coordinates of the acoustic emissions, the crucial step is the picking of the onset. Since there are several thousand acoustic

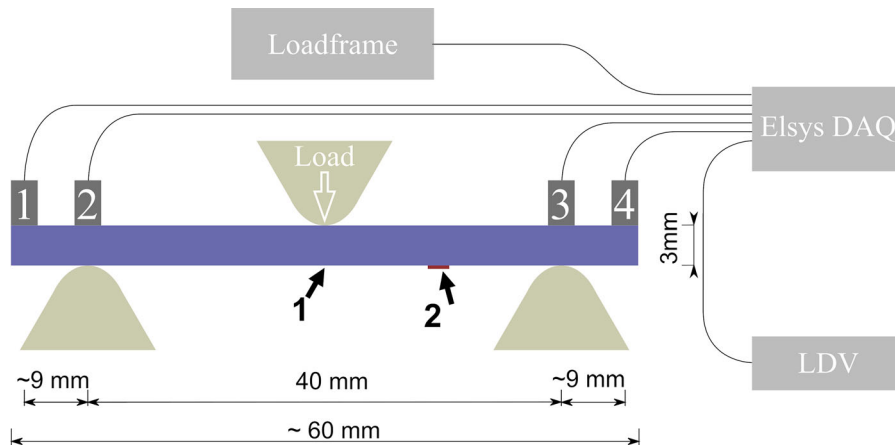


Fig. 4 Experimental setup for static three-point bending tests on miniature beam specimens. Position 1 represents the specimen. A reflective foil for the Laser-Doppler-Vibrometer

is located at position 2. Acoustic emission sensors, numbered from one to four are attached to the edges of the specimen

emission events recorded for each experiment, automated onset picking methods must be applied. In this study, a picking method based on the Akaike Information Criterion (AIC) is used [50]. A first guess for the onset is determined by an adaptive threshold operating on the Hilbert-Transform of the signal, as described in [51]. Provided correct onset times at each sensor, it is possible to calculate event location x_e , phase propagation velocity c and origin time t_0 by solving the equation system given in Eq. (4) in a least-square sense.

$$A|b = \begin{bmatrix} 1 & 1 & -S_{x1} & t_{a1} \\ 1 & 1 & -S_{x2} & t_{a2} \\ 1 & -1 & S_{x3} & t_{a3} \\ 1 & -1 & S_{x4} & t_{a4} \end{bmatrix} \quad (4)$$

S_{xi} denotes the sensor position in x direction and t_{ai} is the arrival time at sensor i . The unknown parameter $a_{1,1}$ correspond to t_0 , $a_{1,2}$ to x_e/c , and $a_{1,2}$ equals to $1/c * S_{x2}$. Thus for every event we obtain the propagation velocity of the respective wave type. Together with the AIC-curvature value (introduced as ‘DD value’ in the literature [50]) the events can be classified into real transient signals and noise or reverberations. The DD value represents the second derivative of the AIC function in the vicinity of the global minimum. Furthermore, a quality estimation of the onset picking process can be derived. Figure 5 shows the relation between event velocity and DD value within a two-dimensional histogram. Events with a DD value above 380 and velocity ranging

between 1000 and 5000 m/s, are highlighted by a blue background and are considered for further processing.

Low velocity events result either from secondary arriving phases, reflections or picking errors. To ensure consistent localization, the velocity for three and four arrival times is calculated. Deviations between those two solutions larger than a 500 m/s are considered as false picks rather than secondary phases. The threshold is derived from stochastic input into the equation system while solving for corrupted synthetic arrival times. When considering the sampling frequency, it was found that cumulative picking errors of 0.5 μ s or 10 samples lead to velocity errors of 1000 m/s. Therefore, 500 m/s is considered as reasonable to avoid false localizations. Following successful source localization, source mechanics can be examined. Research conducted by different authors as indicated in Table 2 (see also e.g. [52]) suggests that the frequency content of acoustic emissions are suitable for failure mode identification. They performed acoustic emission measurements on fiber reinforced materials during different loading regimes and derived relations between frequency and failure modes. Table 2 shows these frequency-to-failure-mode relations from preceding research. The correlations described are supplemented with details on the used sensor equipment and the tested materials. The major influence on the found frequencies is the used sensor technology and the evaluation method.

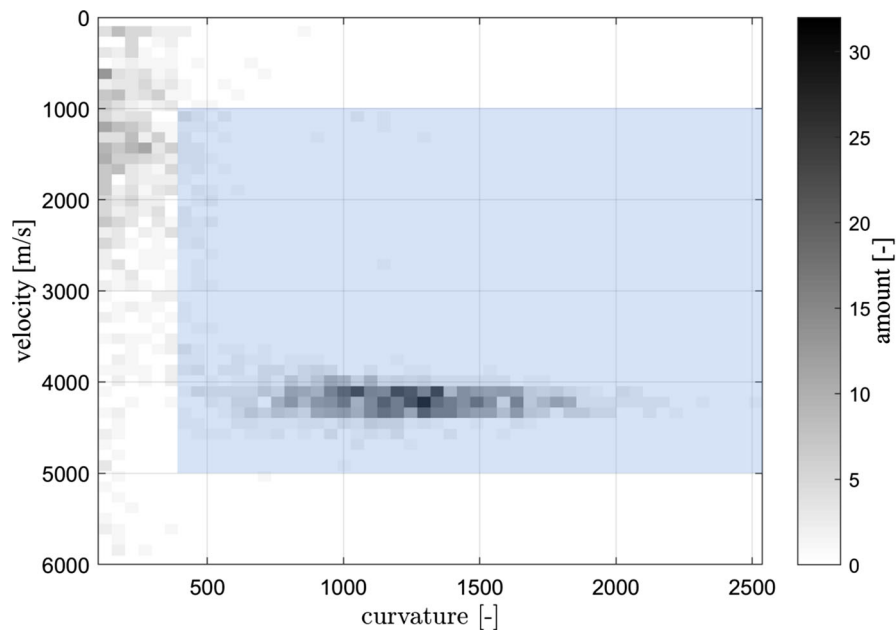


Fig. 5 Velocity and DD value distribution. The blue rectangle marks events which are considered to be single fractures or fibre breakage events. These events are used for further processing

Table 2 Frequency -Failure Mode classification from preceding research

| | Study 1 [53] | Study 2 [54] | Study 3 [55] | Study 4 [56] |
|-----------------|-----------------------|-------------------------|--------------------------|--------------------------|
| Sensor type | WD (PAC) | WD (PAC) | B1025 (DWC) | WD (PAC) |
| Parameter | Peak frequency | Event primary frequency | Time–frequency transform | Time–frequency transform |
| Material | CFRP | GFRP | G/CFRP (epoxy) | Carbon Fiber/Matrix |
| Failure modes | Frequency range [kHz] | | | |
| Matrix cracking | 0–50 | – | 200–300 | 400–500 |
| Fiber pullout | 500–600 | 300 | 700–1100 | – |
| Fiber breakage | 400–500 | 420–520 | > 1500 | 400–1000 |

3 Results

3.1 Fiber alignment

Fiber alignment was measured using pristine miniature bending beams, which were later subjected to bending load. The damaged samples are then scanned again to analyze crack patterns. As X-ray CT scans are reconstructed into a 3-dimensional image, it is possible to analyze the alignment of both in-plane fiber angle (θ -angle) and out-of-plane angle (φ -angle). Figure 1 shows how the sample is oriented for alignment analysis and how description of those

angles is handled. The in-plane alignment (θ -angle) is given as angular deviation from the direction of the occurring tensile force during mechanical testing. Fibers, which are perfectly aligned to the tensile force are given an alignment angle of 0° .

The fibers are segmented according to the procedure laid out in Sect. 2.6. Once a satisfactory segmentation is achieved, the alignment angles can be directly exported from ORS Dragonfly using the ‘connected components analysis’ tool. Excerpts from the tomographic scans showing the overlap between segmented fibers and original scans are provided in the Supplementary Material to this paper. Overall, the

segmented voxels overlap very well with the fibers visible in the X-ray scan. Some oversegmentation can be seen in the form of segmented pores or non-fibrous grains, which might lead to underestimation of the overall alignment, i.e. the segmentation data may artificially suggest a slightly broadened alignment distribution or outliers that do not reflect the actual fibers.

Figure 6 shows the distribution of measured fiber alignment in each template. Figure 6a shows the in-plane alignment (θ -angle), while Fig. 6b shows the out-of-plane alignment (φ -angle). In both cases, the red area of the probability-density distributions represents the 70% quantile around the mode value, while the grey tail-ends represent the 15% highest and lowest values measured. In general, the distributions in Fig. 6a show good correlation between the expected orientation angle defined by the guide lines of the

templates and the measured in-plane orientation values. Figure 6b shows that the out-of-plane alignment occurs mostly parallel to the x–y-plane. The fibers show a φ -angle alignment of mostly 90° , i.e. they show very little upward or downward tilt. In both cases, the 70% quantile suggests that fiber orientation of both angles mainly deviates in the range of $\pm 10^\circ$, which is in good agreement with prior research on this system [15]. Deviations larger than 20° are very rare for both angles, even in samples with a somewhat broader distribution (e.g. the 40° sample).

3.2 Flexural strength

When referencing alignment angles during strength testing, the nomenclature for the in-plane alignment laid out in Fig. 1 is used. A fiber with the alignment angle of 0° is oriented in the same direction as the

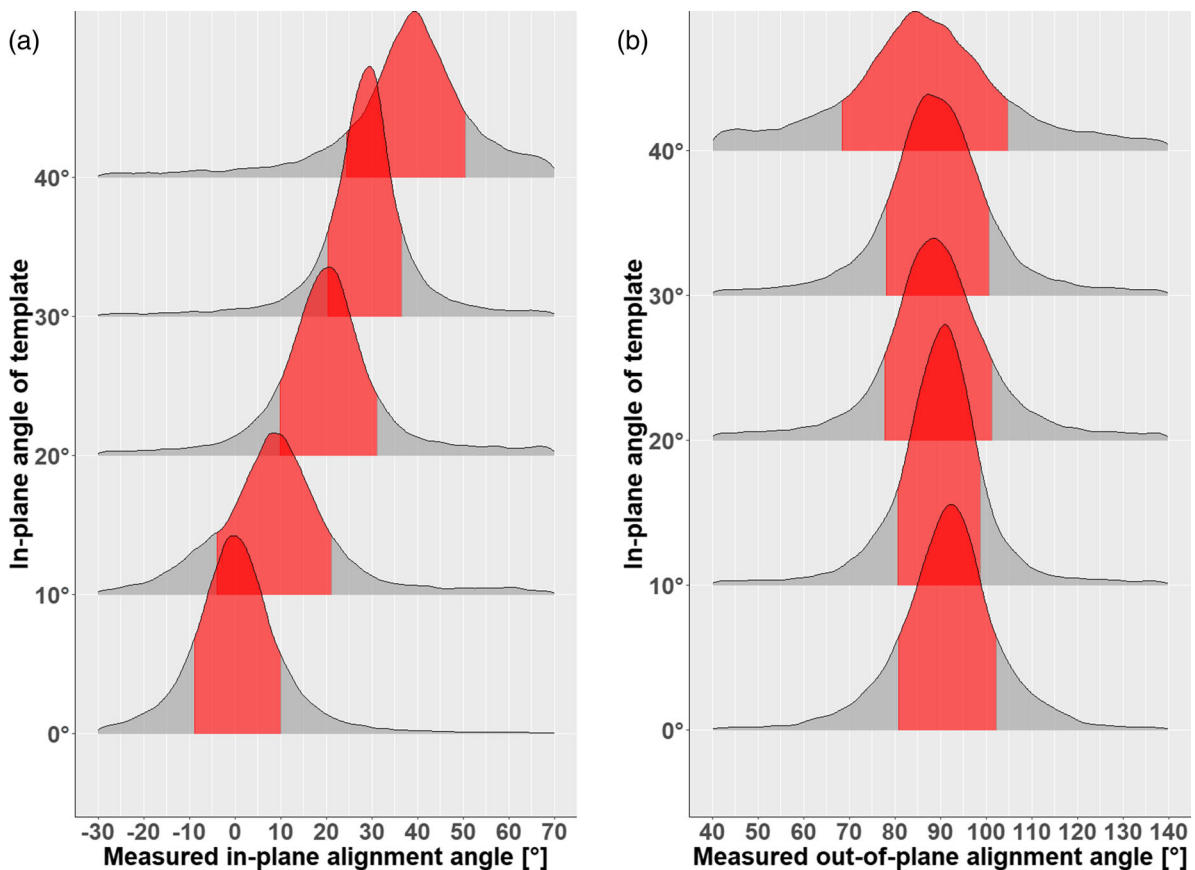


Fig. 6 Distributions of fiber alignment as laid out in Fig. 1. Distribution of **a** in-plane fiber alignment (θ -angle) and **b** out-of-plane fiber alignment (φ -angle). The filled in red area around

mode value of the distribution represents a 70% quantile of well-aligned fibers, while the grey tail-ends represent the 15% lowest and highest values respectively

tensile stress, a fiber with the orientation of 90° is oriented perpendicular to it. Results of the 3-point bending tests can be seen in Fig. 6. Figure 6a shows the stress–strain diagrams of samples containing 1 vol% of carbon fibers, Fig. 6b shows the stress–strain diagrams of samples containing 3 vol% of carbon fibers.

The relation between ultimate flexural strength and fiber alignment angle can be seen in Fig. 6c. On average, samples with a 0° alignment angle containing 3 vol% of fibers show a flexural strength of 107 N/mm^2 and samples containing 1 vol% show a strength of 62 N/mm^2 . Unreinforced samples reach an average strength of 23 N/mm^2 . At alignment angles of 30° , the effects of fiber reinforcement are vastly diminishing, showing nearly fully brittle failure in the sample with 1 vol% fibers (26 N/mm^2) and only moderate reinforcement in the sample with 3 vol% (36 N/mm^2). At angles of 40° the material shows brittle failure for both samples; with values of 19 N/mm^2 the flexural strength is at the level of the unreinforced matrix. As can clearly be seen in the experiments, not only does ultimate flexural strength decrease as the fiber alignment angle shifts away from the direction of the tensile load, but strain at break (and with it the capacity for strain-hardening behavior) shows increasingly lower values as well. While samples at 0° alignment angle can show around 0.8% flexural strain before breaking, this value is already halved to values around 0.4% at angles of 20° (see Fig. 7a, b). Samples with an alignment angle of 40° show a strain at break of around 0.1% or less, which is similar to an unreinforced sample. In contrast to samples without fiber reinforcement, some post cracking behavior (most likely linked to fiber pull-out) can be seen.

The angular dependence of the stress–strain behavior can be quantified theoretically by taking into account that the stress–strain behavior is roughly piecewise linear (cf. Fig. 6a). Starting from an unloaded state, with increasing load, the materials behaves linear-elastically until microcracks begin to appear. When the strain is increased further, single-crack propagation is substantially decreased and the stress–strain relationship behaves roughly linear again until just before failure. Assuming the fiber-volume concentration being small and the fibers being uniformly aligned, the stiffness tensor can be approximated by homogenization techniques or—under further assumptions—by the Mori–Tanaka technique

[57] employing the Eshelby tensor [58], where the short fibers are approximated as prolate ellipsoids, cf. [59] for a recent discussion in the context of short-fiber composites. In the strain-hardening phase, numerical homogenization techniques based on representative volume elements containing fibers and microcracks can be used to compute an approximate stiffness tensor.

If the stiffness tensor for a 0° -orientation in Voigt notation is given by C , then the corresponding stiffness tensor describing the same material but rotated by the angle θ in the x – y -plane can be computed as

$$C_\theta = T_\theta C T_\theta^t \quad (5)$$

with transformation matrix T_θ and the transposed matrix T_θ^t

$$T_\theta = \begin{pmatrix} \cos^2(\theta) & \sin^2(\theta) & 0 & 0 & 0 & 2\sin(\theta)\cos(\theta) \\ \sin^2(\theta) & \cos^2(\theta) & 0 & 0 & 0 & -2\sin(\theta)\cos(\theta) \\ 0 & 0 & 1 & 0 & 0 & 0 \\ 0 & 0 & 0 & \cos(\theta) & -\sin(\theta) & 0 \\ 0 & 0 & 0 & \sin(\theta) & \cos(\theta) & 0 \\ -\sin(\theta)\cos(\theta) & \sin(\theta)\cos(\theta) & 0 & 0 & 0 & \cos^2(\theta) - \sin^2(\theta) \end{pmatrix}^{-1} \quad (6)$$

via simple (but technically involved) coordinate-transformation arguments and by exploiting symmetry properties [60, 61]. Note that this transformation assumes a rotation of the entire material (i.e. representative volume element). This is likely a very good approximation in the undamaged case but less so in the case when microcracks have appeared as their orientation will depend on the direction of the applied stress, which is not rotated with the material.

Furthermore, in the case of an ideal fiber reinforced material with fiber alignment along the x -axis (cf. Fig. 1b), the material can be approximated as transversely isotropic. The corresponding stiffness tensor C is described by only five independent material constants (instead of 21 independent constants in a fully anisotropic material):

$$C = \begin{pmatrix} 1/E_L & -\nu_{12}/E_L & -\nu_{12}/E_L & 0 & 0 & 0 \\ -\nu_{12}/E_L & 1/E_T & -\nu_{23}/E_T & 0 & 0 & 0 \\ -\nu_{12}/E_L & -\nu_{23}/E_T & 1/E_T & 0 & 0 & 0 \\ 0 & 0 & 0 & 1/G_T & 0 & 0 \\ 0 & 0 & 0 & 0 & 1/G_L & 0 \\ 0 & 0 & 0 & 0 & 0 & 1/G_L \end{pmatrix}^{-1} \quad (7)$$

with longitudinal Young's modulus E_L , transverse Young's modulus E_T , ν_{12} Poisson's ratio for loading



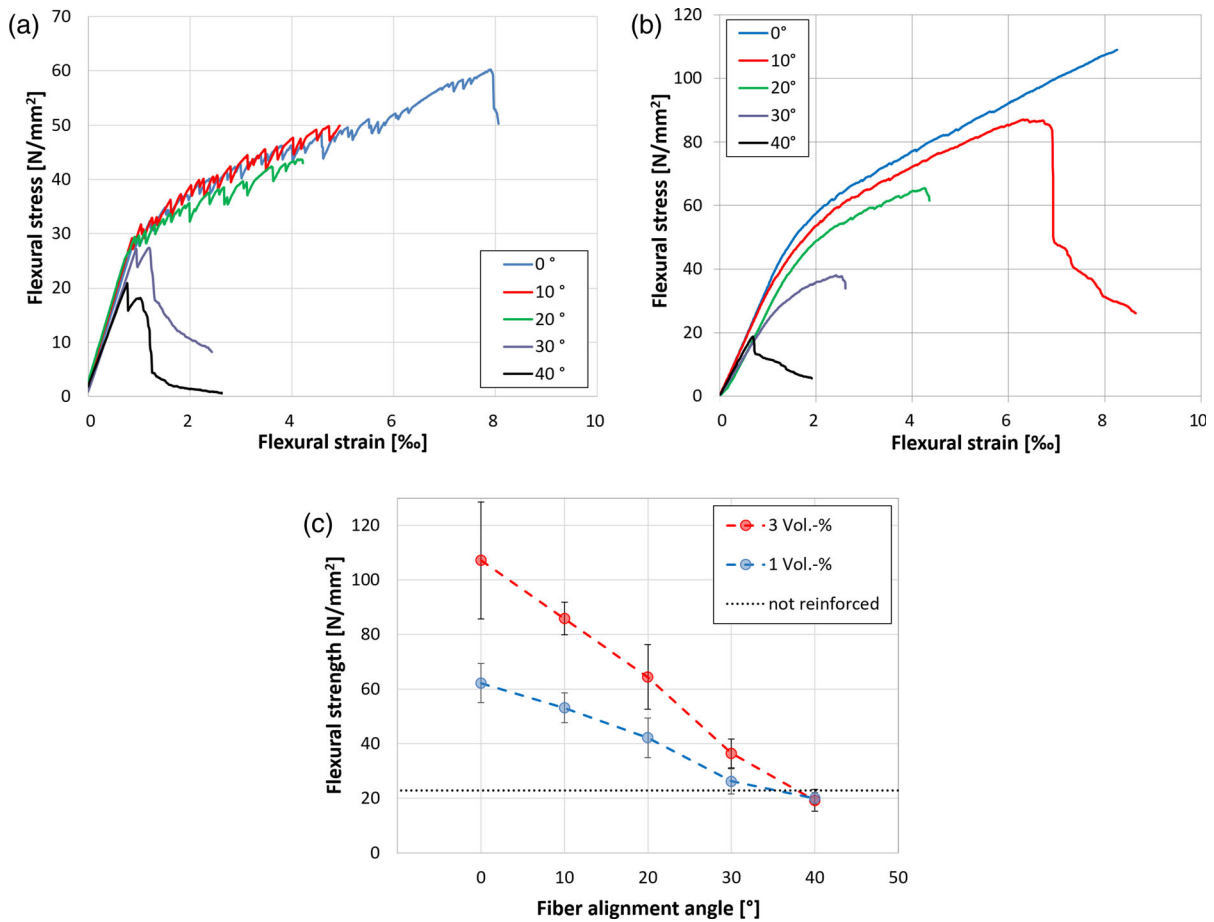


Fig. 7 Stress–strain relationship of miniature beam specimens with a fiber content of: **a** 1 vol% of carbon fibers and **b** 3 vol% of carbon fibers under 3-point bending load at fiber alignment angles between 0° and 40°. **c** Relation between ultimate flexural

strength and alignment angle for fiber contents of 1 vol% (blue) and 3 vol% (red). The dotted black line shows the flexural strength of the unreinforced matrix. (Color figure online)

along the alignment axis x , ν_{23} Poisson's ratio in the plane perpendicular to the preferred direction x , in-plane shear modulus G_T and shear modulus in planes parallel to the preferred direction G_L , and $\nu_{23} = \left(\frac{E_T}{2G_T}\right) - 1$ due to the isotropy assumption. This observation vastly reduces the measurement efforts when fully characterizing the undamaged reinforced concrete and possibly even the damaged material if highly symmetric crack surfaces can be considered a reasonably approximation.

3.3 Visualization of crack patterns on dogbone specimens using digital image correlation

As described before, the plateau in the stress–strain diagram is caused by multi-microcracking over a large area of the specimen (cf. [9, 11, 13]). In sharp contrast to other concrete structures, which show brittle failure and develop a single critical crack, the bridging action of the fibers leads to a state where the formation of a new crack is energetically preferred over the growth of an already existing crack [13]. DIC can serve as a powerful tool in the localized description of such phenomena. Figure 8 shows the behavior of a dogbone specimen under uniaxial tension. The first cracks appear after leaving the linear-elastic phase (point a in Fig. 8a, cracking pattern in image a in Fig. 8b), which

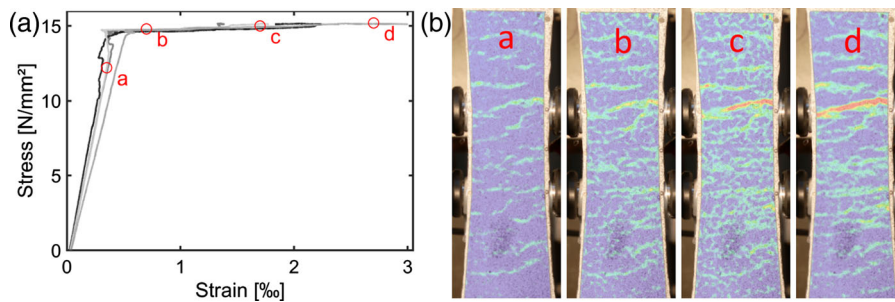


Fig. 8 **a** Stress–strain-relation under uniaxial tension in a dogbone-shaped specimen measured by strain gauges (left) and **b** crack development measured by DIC (right)

then slowly expand and grow until failure, causing further strain in the dogbone while stress only increases minimally (points b–d in Fig. 8a, cracking patterns in the respective images in Fig. 8b). Once the strain-hardening effect has fully set in (points b–d in Fig. 8a), crack spacing is stable at values of around 10–15 mm. The stress–strain-relation during tensile testing can be described as bilinear with huge strain-at-break values caused by a capacity for plastic deformation not present in unreinforced specimens. Unlike the behavior during flexural tests, the first microcracks appear when the stress is already very close to the ultimate strength. Still, there is a large amount of deformation capacity present in the material. These deformations result from elastic strain of the compound matrix and the growth of many microcracks, which further elongate the specimen. The average crack width measured from the image data is about 15 μm , while the maximum crack width shortly before failure is in the range of 30–80 μm .

Looking at a beam specimen with standardized geometry under 3-point bending load, the distance between two cracks stabilizes at values around 4 mm, as seen in Fig. 9b, thus cracks are closer in comparison to the dogbone-shaped samples tested under uniaxial tension. This is due to the fact that during tensile testing the load is distributed evenly across the cross section, whereas 3-point-bending leads to an area with concentrated peak stress directly under the loaded midpoint. Tensile tests are decidedly more sensitive to surface defects or pores, which lead to local stress maxima and subsequently, the first crack. In flexural tests, the load is a lot more concentrated under the point of load application; while macro pores still act as imperfections, the appearance of the first crack is locally much more constricted. Further increase in

stress then forces more cracks to develop along the beam closer to the supports until one of the cracks grows to a fatal size and fiber rupture occurs [35]. The standardized beam geometry shows a lower ultimate flexural strength in comparison to the miniature beam specimens, hinting to either the influence of a size-effect or influences between the different manufacturing processes.

3.4 Acoustic emission analysis

The effect of different fiber orientations is reflected in the number of events as well as in the spatial and temporal distribution of the events, as can be observed in the normalized cumulative events over time for each tested miniature beam specimen (Fig. 10). The event count includes the time from loading start to ultimate failure of the beam, post-cracking behavior is not part of the analysis. The event number is normalized to the event count when the specimen fails. Miniature bending beams with an in-plane alignment of 0° show almost linear growth of event numbers until 80% percent of the total event count. Miniature beams with an in-plane alignment angle of 10° show the linear trend until 50%, reflecting the multiple phases of the stress–strain diagrams. The linear trend is followed by an exponential like growth, signaling impending failure. Higher deviations in alignment don't show linear trends at all, instead an exponential growth starts from the beginning, indicating sudden brittle failure.

The position of the final crack is measured by means of photogrammetry and shown by a red patch on the time position diagram. For miniature beam specimens with an alignment of 0° , the events are distributed lengthwise around a larger area of the

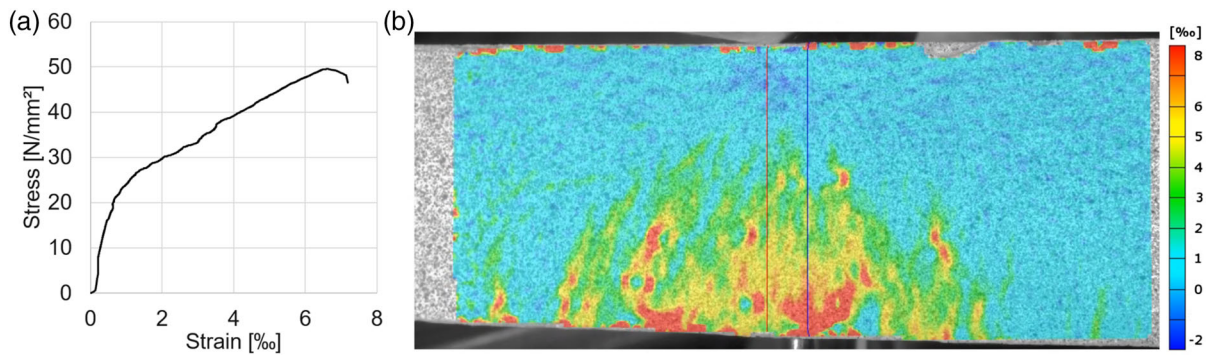


Fig. 9 **a** Stress–strain diagram of a beam with standardized geometry under 3-point bending load, **b** DIC strain distribution in the strain-hardening phase during flexural load shows the wide range of microcracks and the reduction of height of the compression zone

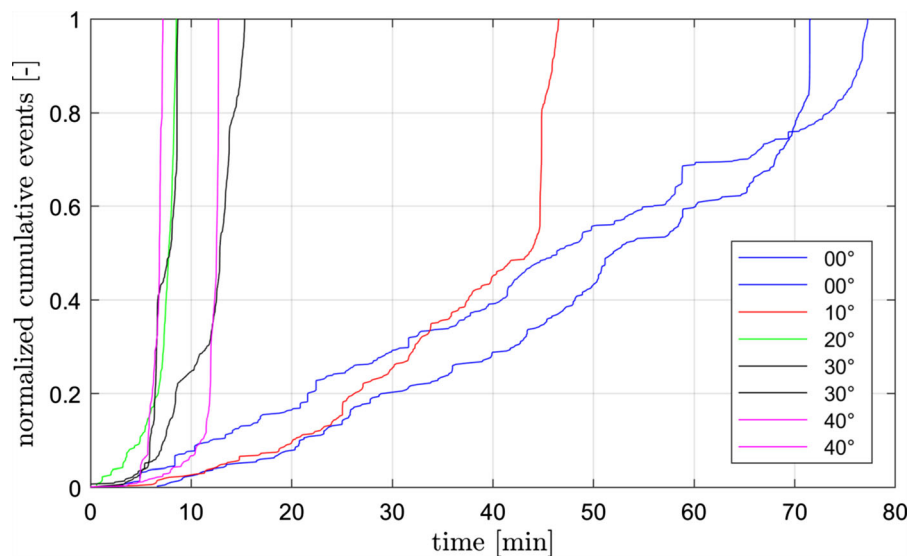


Fig. 10 Normalized cumulative event counts from eight miniature bending beam specimens with a fiber content of 1 vol%. Beams with different in-plane fiber orientations were tested

specimen. In contrast, deviating angles show the events concentrated around the final crack position. This is especially visible before maximum load is reached as in Fig. 11a. Dye penetration tests show different fracture patterns for different fiber orientations. A comparison between the distribution of spatial events and crack pattern for a miniature beam with an in-plane-alignment angle of 0° is given in Fig. 11a. The spatial event distribution and the fracture positions match and show a bimodal distribution around the final crack. Event clusters are distributed between 27 and 37 mm, whereas results for miniature beams with an in-plane alignment angle of 40° deviate clearly (see Fig. 11b). The event distribution follows a

unimodal distribution around the final fracture, which is reflected by the absence of visible fractures from dye penetration test. When disregarding single events, as shown in the histogram, the majority of all events are localized between 36 and 40.2 mm. The majority of all events is therefore within a range of two millimeters around the fatal crack. This distribution can either be attributed to uncertainty in localization or to the extent of fibers outside the crack and fiber pullout events.

Based on the temporal distribution, it can be stated that first event clusters are not necessarily attributed to the fatal fracture. Instead, as seen in the experiments and also described elsewhere in the literature, fractures

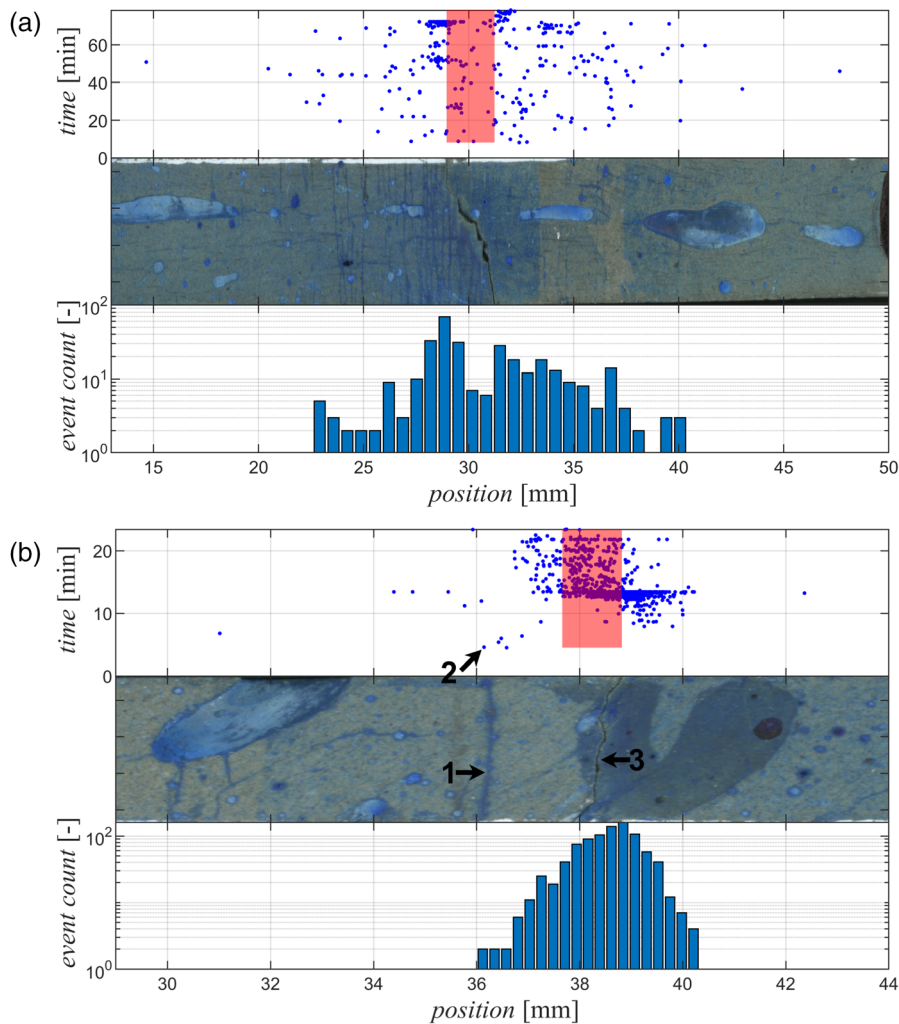


Fig. 11 **a** Spatial and temporal event distribution for a miniature beam with 0° fiber orientation. The region marked in red indicates the dimensions of the fatal fracture. **b** Spatial and temporal event distribution for miniature beams with 40° fiber

orientation. Position 2 marks first localized events which correspond to the crack marked at position 1. Marker 3 is pointing to the fatal crack

can develop later in the loading process [62]. This suggests that several flaws within the material cumulate to a major crack while other initial cracks and crack branches die out. This effect can be seen clearly in Fig. 11b, where the crack at position 1 produced the first localized events (2) in the experiment.

Displacement signals captured by the LDV were decomposed into a frequency-time representation using a continuous wavelet transformation and a Gabor wavelet. Thus, the temporal occurrence of different frequencies becomes visible. Figure 12 shows characteristic events representing different

frequency contents. Figure 12 provides characteristic signals, with increasing frequency content. The lowest frequencies shown in Fig. 12a can be linked to extended matrix cracking whereas the higher frequencies can be attributed to different mechanisms. Fiber fracture is generally attributed to high frequency content, and thus the signal in Fig. 12d is considered to be a fiber fracture. Figure 12b, c show intermediate frequencies which can be assigned to fiber pull out events. All signals exhibit large amplitudes at 85 kHz which probably stem from specimen eigenfrequencies. In order to distinguish between different fracture

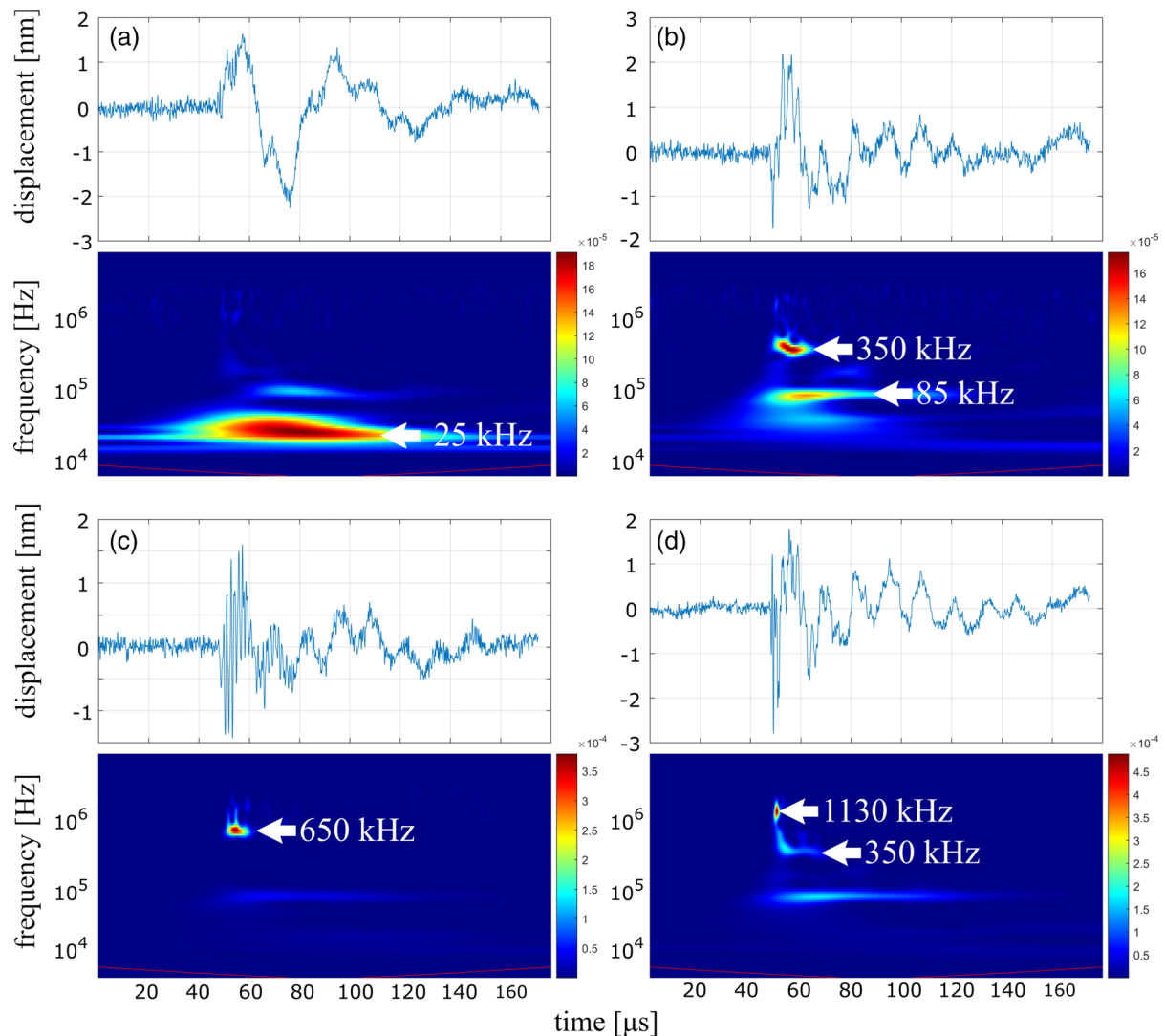


Fig. 12 Selection of characteristic AE signals, which were recorded on a miniature beam with an alignment of 40° . The signals are arranged in ascending frequency content from (a–d). **a** Example of a low frequency signal with maximum amplitudes at 25 kHz and is considered a matrix fracture event. **b** Significant

amplitudes at 85 and 350 kHz, whereas 85 kHz is regarded to be a resonance within the specimen. **c** Signal with dominant frequency around 650 kHz can be attributed to fiber pullout. The highest frequency components recorded within the experiments are probably associated with fiber breakage are shown in (d)

modes and eigenfrequencies, modal analysis measurements are required and will be considered in future studies.

During the experiment, the specimen will change its exact position and orientation relative to the fixed laser beam. Thus, the movement of the specimen leads to a change in the reflectivity of the laser and therefore a change in the Green's function. As a consequence, some signals are superimposed by heavy noise and cannot be analyzed. Therefore, a statistical approach

for data analysis is not feasible and therefore this work is limited to a phenomenological representation of the results. As outcome of the frequency analysis the following three observations can be reported:

- Most of the recorded events seem to include more than one fracture mechanism in the time frame of the transient signal and therefore, combined processes of matrix- and fiber fracture must be considered.

- Fiber breakage and pullout can be detected and can possibly be distinguished on frequency basis.

3.5 Damage patterns and crack spacing segmented using X-ray CT

X-ray CT scans were carried out on miniature bending beams with a fiber content of 1 vol%. The results of the acoustic emission analysis indicate that the main fracture processes occur symmetrically around the loaded area at the midpoint of the miniature bending beams. Thus, an area of about 12 mm along the fracture zone is scanned during X-ray CT measurements and the damage is segmented.

Usually, the fiber-reinforced miniature beams will not be completely split in two after failure and stay connected over a small area in the compressive zone. The process zone of samples that stay in one piece is scanned directly in the tomograph. For all following figures, the fatal crack is always visualized in red, while non-fatal microcracks are shown in teal. In the case of the miniature beam with 0° fiber alignment angle, the miniature beam split completely during testing, thus each half of the beam was scanned separately and the main crack is shown as an unsegmented large gap with only the microcracks being segmented and displayed in teal color.

Analysis of microstructural damage confirms the effects also seen in the AE tests. The strain-hardening response diminishes as seen in decreasing strain-at-break values the more fiber alignment deviates from the direction of the occurring tensile stress. Also, transmission of stress onto the fibers becomes gradually worse and thus cracks cannot be effectively bridged anymore, leading to the sharp decrease in flexural strength and strain-at-break values seen in Fig. 7. As a consequence, fewer microcracks can be observed in the specimen. The sample with 0° alignment angle (Fig. 13a) shows multiple, very closely spaced microcracks in its process zone. At a 10° deviation in alignment (Fig. 13b), the number of observable cracks is already more than halved. At 20° angular deviation (Fig. 13c), only 3 cracks remain visible. For the samples with alignment angles of 30° and 40° (Fig. 13d, e), only one crack could be observed within the process zone, showing that the fiber reinforcement is no longer capable of bearing the tensile load and explaining the brittle behavior of the

specimens. A brief quantitative approach to measuring crack distances from the CT datasets can be found in the Supplementary Material to this paper.

4 Conclusion

Additions of chopped carbon fibers leads to a strain-hardening cementitious material, the mechanical performance of which is intrinsically linked to its microcracking behavior. Alignment of carbon fibers during the extrusion process, by which test specimens are prepared, leads to an altered fracture process. Microcracks bridged by fibers demand higher energy to propagate further, rendering formation of new cracks energetically more favorable [63]. Thus, the material no longer shows sudden single-crack brittle failure, but rather pseudoductility and multiple cracking. Transmission of tensile load from the cementitious matrix to the fiber leads to significantly increased tensile and flexural strength.

Since acoustic emission analysis (AEA) is directly related to the cracking behaviour, appropriate measuring techniques have been applied based on former experimental investigations studying fiber reinforced concrete [34]. As one of only a few non-destructive testing techniques, AEA is able to investigate the spatiotemporal development of deteriorations like fiber breaking and matrix cracks. Signal-based techniques have been applied including a 1D location based on linear least squares and an automatic picking algorithm (AIC). A modified technique for the discrimination between noise and AE signals was used. To perform higher-order signal investigations, a LDV was additionally used for evaluations of the signal frequency content including wavelet transforms [64]. The application of the LDV-technique enabled for a recording of the true ground motion (and not normalized amplitudes only) originating from the emitted AE waves. In further studies, with adapted specimen geometries, this will be used to derive the true seismic moment [65] of the cracks and therefore the real size of the crack and the released energy can be calculated. This will in future be performed along with applications of ultrasound techniques including coda wave interferometry (CWI) [66]. CWI was already applied but the number of data was yet too little to be processed in a reliable way. Another promising approach tested elsewhere at the time being is the

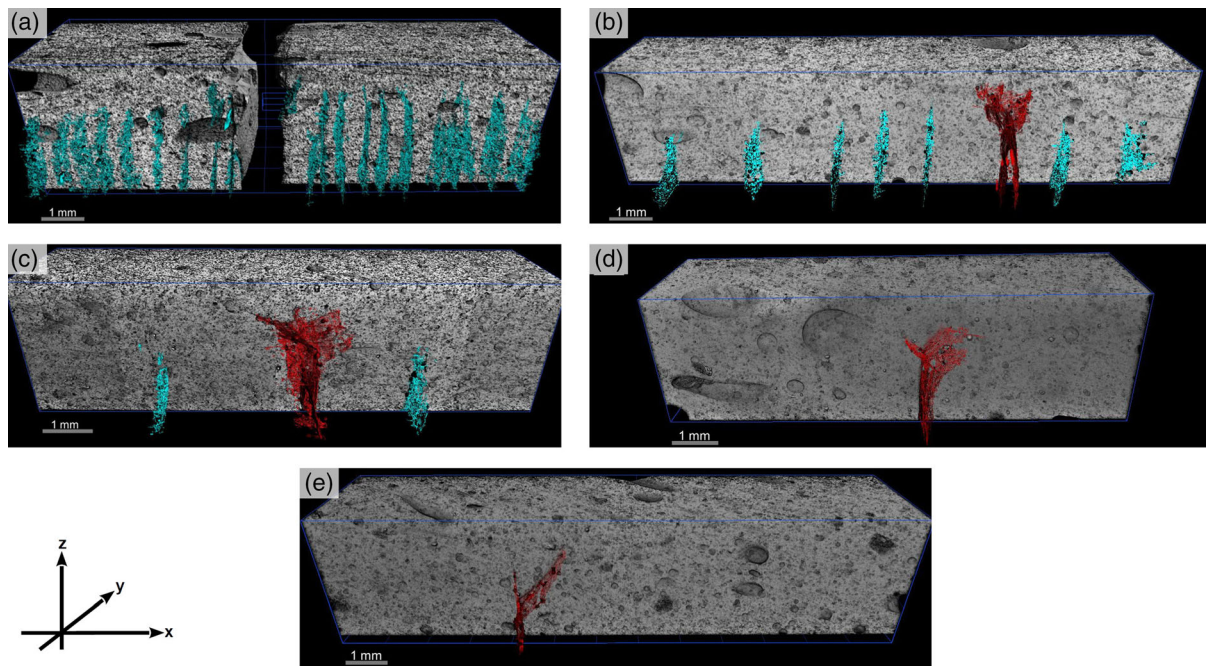


Fig. 13 Cracking patterns in miniature bending beams with a fiber content of 1 vol%. In-plane alignment angles in the samples are **a** 0°, **b** 10°, **c** 20°, **d** 30° and **e** 40° as defined in Fig. 1. The figures show a side view on the samples, with about

1 mm of the sample digitally removed to high-light crack progression. The fatal crack is shown in red, non-fatal microcracks are shown in teal color. The 0° sample separated completely during testing, the fatal crack is shown as large gap

use of an etalon-based optical microphone for the detection of acoustic waves in a non-contact way [67].

Extrusion of the fibrous paste through a tight nozzle allows for excellent control of fiber alignment; CT measurement show a number of 70% of well-aligned fibers, which is close to numbers reported elsewhere on this system. Microcracking during loading can be seen in stress–strain curves as a strain-hardening phase, the process is very well observable by means of DIC and acoustic emission. X-ray CT scans taken after failure confirm the processes seen in the aforementioned methods. The strength of the material and the amount of microcracks formed correlates strongly with alignment of fibers in direction of occurring tensile forces. As fiber alignment deviates, both pseudoductility and strength decrease, indicating that transmission of tensile load from matrix to fiber gets worse. The reduced transmission of loads leads to a vastly reduced capability for microcracking in the material and thus a change from ductile to brittle material behavior. Effects of the reinforcement can be observed up until an angular deviation of 20°, at 30°

hardly any effects and at 40° no effects of an effective reinforcement can be seen anymore.

Acknowledgements The researchers extend their gratitude to everyone involved in the priority programme SPP 2020, as the working atmosphere between the groups is shaped by a sense of fruitful collaboration. The Chair of Solid State and Materials Chemistry thanks Schwenk Zement KG for kindly supplying the cement used in this research.

Authors contributions *Chair of Solid State and Materials Chemistry:* X-ray 3D computed tomography scans and image analysis, development of optimized mixture design, preparation and flexural tests on small beam specimens. *Chair of Concrete & Masonry Structures:* Preparation, tensile and flexural testing of larger specimens. Analysis via digital image correlation. *Chair of Non-Destructive Testing:* Acoustic emission analysis of small beam specimens under flexural load. *Research Unit Applied Analysis:* Theoretical background concerning modeling of carbon fiber alignment-dependent properties.

Funding Open Access funding enabled and organized by Projekt DEAL. This research was funded by the German Research Foundation DFG as part of the ‘Priority Programme SPP 2020: Cyclic deterioration of High-Performance Concrete in an experimental-virtual lab’ (Grant Numbers VO 829/13-1, FI 1720/7-1, GR1664/13-1, PE 1464/6-1).

Availability of data and materials Raw data is available from the authors upon request.

Code availability Not applicable.

Compliance with ethical standards

Conflict of interest The authors declare that they have no conflict of interest.

Open Access This article is licensed under a Creative Commons Attribution 4.0 International License, which permits use, sharing, adaptation, distribution and reproduction in any medium or format, as long as you give appropriate credit to the original author(s) and the source, provide a link to the Creative Commons licence, and indicate if changes were made. The images or other third party material in this article are included in the article's Creative Commons licence, unless indicated otherwise in a credit line to the material. If material is not included in the article's Creative Commons licence and your intended use is not permitted by statutory regulation or exceeds the permitted use, you will need to obtain permission directly from the copyright holder. To view a copy of this licence, visit <http://creativecommons.org/licenses/by/4.0/>.

References

- Larisa U, Solbon L, Sergei B (2017) Fiber-reinforced concrete with mineral fibers and nanosilica. *Procedia Eng* 195:147–154. <https://doi.org/10.1016/j.proeng.2017.04.537>
- Iskender M, Karasu B (2018) Glass fibre reinforced concrete (GFRC). *ECJSE* 5(1):136–162. <https://doi.org/10.31202/ecjse.371950>
- Li VC, Wang S, Wu C (2001) Tensile strain-hardening behavior of polyvinyl alcohol engineered cementitious composite (PVA-ECC). *ACI Mater J* 98(6):483–492
- Banthia N, Sappakittipakorn M (2007) Toughness enhancement in steel fiber reinforced concrete through fiber hybridization. *Cem Concr Res* 37(9):1366–1372. <https://doi.org/10.1016/j.cemconres.2007.05.005>
- Brückner A, Ortlepp R, Curbach M (2006) Textile reinforced concrete for strengthening in bending and shear. *Mater Struct* 39(8):741–748. <https://doi.org/10.1617/s11527-005-9027-2>
- Lochner T, Peter MA (2020) Homogenization of linearized elasticity in a two-component medium with slip displacement conditions. *J Math Anal Appl* 483(2):123648. <https://doi.org/10.1016/j.jmaa.2019.123648>
- Fu S, Lauke B (1996) Effects of fiber length and fiber orientation distributions on the tensile strength of short-fiber-reinforced polymers. *Compos Sci Technol* 56(10):1179–1190. [https://doi.org/10.1016/S0266-3538\(96\)00072-3](https://doi.org/10.1016/S0266-3538(96)00072-3)
- Zollo RF (1997) Fiber-reinforced concrete: an overview after 30 years of development. *Cem Concr Compos* 19(2):107–122. [https://doi.org/10.1016/S0958-9465\(96\)00046-7](https://doi.org/10.1016/S0958-9465(96)00046-7)
- Li VC (2003) On engineered cementitious composites (ECC). *J Adv Concr Technol* 1(3):215–230. <https://doi.org/10.3151/jact.1.215>
- van Zijl GP (2007) Improved mechanical performance: Shear behaviour of strain-hardening cement-based composites (SHCC). *Cem Concr Res* 37(8):1241–1247. <https://doi.org/10.1016/j.cemconres.2007.04.009>
- Li VC, Leung CKY (1992) Steady-state and multiple cracking of short random fiber composites. *J Eng Mech* 118(11):2246–2264. [https://doi.org/10.1061/\(ASCE\)0733-9399\(1992\)118:11\(2246\)](https://doi.org/10.1061/(ASCE)0733-9399(1992)118:11(2246))
- Jun P, Mechtcherine V (2010) Behaviour of strain-hardening cement-based composites (SHCC) under monotonic and cyclic tensile loading. *Cem Concr Compos* 32(10):801–809. <https://doi.org/10.1016/j.cemconcomp.2010.07.019>
- Kanada T, Li VC (1998) Multiple cracking sequence and saturation in fiber reinforced cementitious composites. *Concr Res Technol* 9(2):19–33
- Curosu I, Mechtcherine V, Forni D et al (2017) Performance of various strain-hardening cement-based composites (SHCC) subject to uniaxial impact tensile loading. *Cem Concr Res* 102:16–28. <https://doi.org/10.1016/j.cemconres.2017.08.008>
- Hambach M, Volkmer D, Möller H et al (2016) Portland cement paste with aligned carbon fibers exhibiting exceptionally high flexural strength (> 100 MPa). *Cem Concr Res* 89:80–86. <https://doi.org/10.1016/j.cemconres.2016.08.011>
- Hambach M, Volkmer D (2017) Properties of 3D-printed fiber-reinforced Portland cement paste. *Cem Concr Compos* 79:62–70. <https://doi.org/10.1016/j.cemconcomp.2017.02.001>
- Paul SC, van Zijl GP (2016) Chloride-induced corrosion modelling of cracked reinforced SHCC. *Arch Civ Mech Eng* 16(4):734–742. <https://doi.org/10.1016/j.acme.2016.04.016>
- Sherir MA, Hossain KM, Lachemi M (2016) Self-healing and expansion characteristics of cementitious composites with high volume fly ash and MgO-type expansive agent. *Constr Build Mater* 127:80–92. <https://doi.org/10.1016/j.conbuildmat.2016.09.125>
- Zhang P, Dai Y, Ding X et al (2018) Self-healing behaviour of multiple microcracks of strain hardening cementitious composites (SHCC). *Constr Build Mater* 169:705–715. <https://doi.org/10.1016/j.conbuildmat.2018.03.032>
- Li VC, Herbert E (2012) Robust Self-Healing Concrete for Sustainable Infrastructure. *J Adv Concr Technol* 10(6):207–218. <https://doi.org/10.3151/jact.10.207>
- Hambach M, Volkmer D, Möller H et al (2016) Carbon fibre reinforced cement-based composites as smart floor heating materials. *Compos B Eng* 90:465–470. <https://doi.org/10.1016/j.compositesb.2016.01.043>
- Chung D (2000) Cement reinforced with short carbon fibers: a multifunctional material. *Compos B Eng* 31(6–7):511–526. [https://doi.org/10.1016/S1359-8368\(99\)00071-2](https://doi.org/10.1016/S1359-8368(99)00071-2)
- Soltan DG, Li VC (2018) A self-reinforced cementitious composite for building-scale 3D printing. *Cem Concr Compos* 90:1–13. <https://doi.org/10.1016/j.cemconcomp.2018.03.017>
- Lewicki JP, Rodriguez JN, Zhu C et al (2017) 3D-printing of meso-structurally ordered carbon fiber/polymer composites



- with unprecedented orthotropic physical properties. *Sci Rep* UK 7:43401. <https://doi.org/10.1038/srep43401>
25. Kanarska Y, Duoss EB, Lewicki JP et al (2019) Fiber motion in highly confined flows of carbon fiber and non-Newtonian polymer. *J Non-Newton Fluid* 265:41–52. <https://doi.org/10.1016/j.jnnfm.2019.01.003>
 26. Maiti A, Small W, Lewicki JP et al (2016) 3D printed cellular solid outperforms traditional stochastic foam in long-term mechanical response. *Sci Rep* UK 6:24871. <https://doi.org/10.1038/srep24871>
 27. Fischer O, Volkmer D, Lauff P et al (2019) Zementgebundener kohlenstofffaserverstärkter Hochleistungswerkstoff (Carbonkurzfaserbeton). *Forschungsinitiative Zukunft Bau*, F 3178. Fraunhofer IRB Verlag, Stuttgart
 28. Khoshnevis B, Dutton R (1998) Innovative rapid prototyping process makes large sized, smooth surfaced complex shapes in a wide variety of materials. *Mater Technol* 13(2):53–56. <https://doi.org/10.1080/10667857.1998.11752766>
 29. Pegna J (1995) Application of cementitious bulk materials to site processed solid freeform construction
 30. Tay YWD, Panda B, Paul SC et al (2017) 3D printing trends in building and construction industry: a review. *Virtual Phys Prototyping* 12(3):261–276. <https://doi.org/10.1080/17452759.2017.1326724>
 31. de Schutter G, Lesage K, Mechtcherine V et al (2018) Vision of 3D printing with concrete—technical, economic and environmental potentials. *Cem Concr Res* 112:25–36. <https://doi.org/10.1016/j.cemconres.2018.06.001>
 32. Mechtcherine V, Nerella VN, Will F et al (2019) Large-scale digital concrete construction—CONPrint3D concept for on-site, monolithic 3D-printing. *Autom Constr* 107:102933. <https://doi.org/10.1016/j.autcon.2019.102933>
 33. Nerella VN, Ogura Hiroki, Mechtcherine V (2018) Incorporating reinforcement into digital concrete construction. In: *The annual symposium of the IASS—international association for shell and spatial structures: creativity in structural design*
 34. Busse G, Kröplin B, Wittel FK (2006) Damage and its evolution in fiber-composite materials. In: Busse G, Kröplin B-H, Wittel FK (eds) *Simulation and non-destructive evaluation*. University of Stuttgart, Stuttgart
 35. Lauff P, Fischer O (2019) Effizienter Ultrahochleistungsbeton mit innovativer trajektorienorientierter „Bewehrung“. *ce/papers* 3(2):82–88. <https://doi.org/10.1002/cepa.976>
 36. Schneider K, Lieboldt M, Liebscher M et al (2017) Mineral-based coating of plasma-treated carbon fibre rovings for carbon concrete composites with enhanced mechanical performance. *Materials* (Basel, Switzerland). <https://doi.org/10.3390/ma10040360>
 37. Hambach M (2017) *Hochfeste multifunktionale Verbundwerkstoffe auf Basis von Portlandzement und Kohlenstoffkurzfasern*. Thesis, Universität Augsburg
 38. Carrara P, Kruse R, Bentz DP et al (2018) Improved mesoscale segmentation of concrete from 3D X-ray images using contrast enhancers. *Cem Concr Compos* 93:30–42. <https://doi.org/10.1016/j.cemconcomp.2018.06.014>
 39. McCormick N, Lord J (2010) Digital image correlation. *Mater Today* 13(12):52–54. [https://doi.org/10.1016/S1369-7021\(10\)70235-2](https://doi.org/10.1016/S1369-7021(10)70235-2)
 40. Alam SY, Saliba J, Loukili A (2014) Fracture examination in concrete through combined digital image correlation and acoustic emission techniques. *Constr Build Mater* 69:232–242. <https://doi.org/10.1016/j.conbuildmat.2014.07.044>
 41. Baril MA, Sorelli L, Réthoré J et al (2016) Effect of casting flow defects on the crack propagation in UHPFRC thin slabs by means of stereovision Digital Image Correlation. *Constr Build Mater* 129:182–192. <https://doi.org/10.1016/j.conbuildmat.2016.10.102>
 42. Oesch T, Landis E, Kuchma D (2018) A methodology for quantifying the impact of casting procedure on anisotropy in fiber-reinforced concrete using X-ray CT. *Mater Struct* 51(3):1464. <https://doi.org/10.1617/s11527-018-1198-8>
 43. Kronenberger M, Schladitz K, Hamann B et al (2018) Fiber segmentation in crack regions of steel fiber reinforced concrete using principal curvature. *Image Anal Stereol* 37(2):127. <https://doi.org/10.5566/ias.1914>
 44. Dassios KG, Aggelis DG, Kordatos EZ et al (2013) Cyclic loading of a SiC-fiber reinforced ceramic matrix composite reveals damage mechanisms and thermal residual stress state. *Compos A Appl S* 44:105–113. <https://doi.org/10.1016/j.compositesa.2012.06.011>
 45. Arumugam V, Kumar CS, Santulli C et al (2013) Identification of failure modes in composites from clustered acoustic emission data using pattern recognition and wavelet transformation. *Arab J Sci Eng* 38(5):1087–1102. <https://doi.org/10.1007/s13369-012-0351-x>
 46. Reinhardt H-W, Grosse CU, Weiler B (2001) Material characterization of steel fibre reinforced concrete using neutron CT, ultrasound and quantitative acoustic emission techniques. *NDT.net* 6(5)
 47. Radlmeier M, Jahnke P, Grosse CU (2012) Failure mechanisms of carbon-fiber-reinforced polymer materials characterized by acoustic emission techniques. In: *30th European conference on acoustic emission testing & 7th international conference on acoustic emission*
 48. Grosse CU, Goldammer M, Grager JC, Heichler G et al (2016) Comparison of NDT techniques to evaluate CFRP—results obtained in a MAIZfp round robin test. In: *19th world conference on nondestructive testing*
 49. Grosse CU, Linzer LM (2008) Signal-based AE analysis. In: Grosse CU, Ohtsu M (eds) *Acoustic emission testing*. Springer, Berlin, pp 53–99
 50. Maeda N (1985) A method for reading and checking phase time in auto-processing system of seismic wave data. *Zisinl* 38(3):365–379. https://doi.org/10.4294/zisin1948.38.3_365
 51. Kurz JH, Grosse CU, Reinhardt H-W (2005) Strategies for reliable automatic onset time picking of acoustic emissions and of ultrasound signals in concrete. *Ultrasonics* 43(7):538–546. <https://doi.org/10.1016/j.ultras.2004.12.005>
 52. Niemz P, Cesca S, Heimann S et al (2020) Full-waveform-based characterization of acoustic emission activity in a mine-scale experiment: a comparison of conventional and advanced hydraulic fracturing schemes. *Geophys J Int* 222(1):189–206. <https://doi.org/10.1093/gji/ggaa127>
 53. Gutkin R, Green CJ, Vangrattanachai S et al (2011) On acoustic emission for failure investigation in CFRP: Pattern recognition and peak frequency analyses. *Mech Syst Signal*



- Process 25(4):1393–1407. <https://doi.org/10.1016/j.ymssp.2010.11.014>
54. Ramirez-Jimenez C, Papadakis N, Reynolds N et al (2004) Identification of failure modes in glass/polypropylene composites by means of the primary frequency content of the acoustic emission event. *Compos Sci Technol* 64(12):1819–1827. <https://doi.org/10.1016/j.compscitech.2004.01.008>
 55. Jong H-J (2006) Transverse cracking in a cross-ply composite laminate—detection in acoustic emission and source characterization. *J Compos Mater* 40(1):37–69. <https://doi.org/10.1177/0021998305053507>
 56. Sause MGR, Richler S (2015) Finite element modelling of cracks as acoustic emission sources. *J Nondestruct Eval* 34(1):10. <https://doi.org/10.1007/s10921-015-0278-8>
 57. Mori T, Tanaka K (1973) Average stress in matrix and average elastic energy of materials with misfitting inclusions. *Acta Metall* 21(5):571–574. [https://doi.org/10.1016/0001-6160\(73\)90064-3](https://doi.org/10.1016/0001-6160(73)90064-3)
 58. Eshelby JD (1957) The determination of the elastic field of an ellipsoidal inclusion, and related problems. *Proc R Soc Lond A* 241(1226):376–396. <https://doi.org/10.1098/rspa.1957.0133>
 59. Babu KP, Mohite PM, Upadhyay CS (2018) Development of an RVE and its stiffness predictions based on mathematical homogenization theory for short fibre composites. *Int J Solids Struct* 130–131:80–104. <https://doi.org/10.1016/j.ijsolstr.2017.10.011>
 60. Zorn H (2017) Optimierung der Materialausrichtung von orthotropen Materialien in Schalenkonstruktionen. Universität Trier, Trier
 61. Altenbach H, Altenbach J, Kissing W (2004) Mechanics of composite structural elements. Springer, Berlin
 62. Yu J (2019) Why nominal cracking strength can be lower for later cracks in strain-hardening cementitious composites with multiple cracking? In: Proceedings of the 10th international conference on fracture mechanics of concrete and concrete structures. IA-FraMCoS
 63. Kanda T, Li VC (2006) Practical design criteria for saturated pseudo strain hardening behavior in ECC. *J Adv Concr Technol* 4(1):59–72. <https://doi.org/10.3151/jact.4.59>
 64. Hamstad MA, O’Gallagher A, Gary J (2002) A wavelet transform applied to acoustic emission signals: part 1: source identification. *IAE* 20:39–61
 65. Aki K, Richards PG (2002) Quantitative seismology, 2nd edn. University Science Books, Sausalito
 66. Wang X, Chakraborty J, Bassil A et al (2020) Detection of multiple cracks in four-point bending tests using the coda wave interferometry method. *Sensors* (Basel, Switzerland). <https://doi.org/10.3390/s20071986>
 67. Rus J, Grosse CU (2020) Local ultrasonic resonance spectroscopy: a demonstration on plate inspection. *J Nondestruct Eval* 39(2):154. <https://doi.org/10.1007/s10921-020-00674-5>

Publisher’s Note Springer Nature remains neutral with regard to jurisdictional claims in published maps and institutional affiliations.

